Cell Reports

Resource

Super-Resolution Mapping of Neuronal Circuitry With an Index-Optimized Clearing Agent

Graphical Abstract

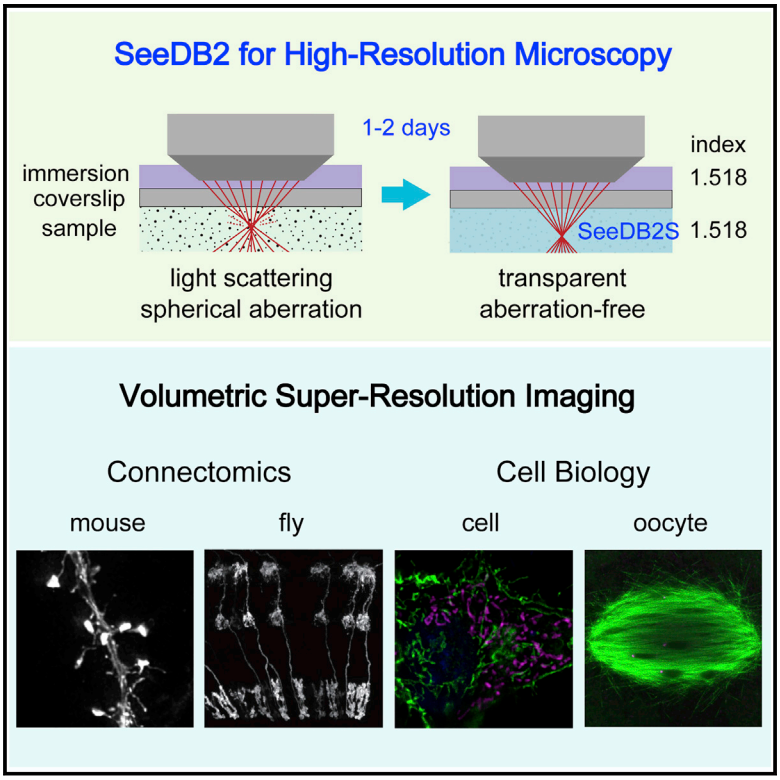

Highlights

- SeeDB2 is a simple optical clearing method preserving morphology and fluorophores
- SeeDB2 is optimized for high-resolution imaging by minimizing spherical aberrations
- Volumetric super-resolution imaging enables synaptic-scale connectomic studies
- Quantitative synapse mapping is demonstrated for mouse and fly brain samples

Authors

Meng-Tsen Ke, Yasuhiro Nakai, Satoshi Fujimoto, ..., Tomoya S. Kitajima, Makoto Sato, Takeshi Imai

Correspondence

imai@cdb.riken.jp

In Brief

Ke et al. have developed a tissue-clearing agent for high-resolution fluorescence microscopy (SeeDB2). Combined with super-resolution microscopy, SeeDB2 allows large-scale synaptic mapping of thick brain tissues, facilitating light-microscopy-based connectomics. Using this approach, the authors reveal synaptic organization of neurons in both the *Drosophila* and mouse brain.

Ke et al., 2016, Cell Reports *14*, 2718–2732
March 22, 2016
http://dx.doi.org/10.1016/j.celrep.2016.02.057

CellPress

OPEN ACCESS
CellPress

Cell Reports
Resource

Super-Resolution Mapping of Neuronal Circuitry With an Index-Optimized Clearing Agent

Meng-Tsen Ke,[1] Yasuhiro Nakai,[3,5] Satoshi Fujimoto,[1] Rie Takayama,[3,5] Shuhei Yoshida,[2] Tomoya S. Kitajima,[2,7] Makoto Sato,[3,4,5] and Takeshi Imai[1,6,7,*]
[1]Laboratory for Sensory Circuit Formation
[2]Laboratory for Chromosome Segregation
RIKEN Center for Developmental Biology, Kobe 650-0047, Japan
[3]Laboratory of Developmental Neurobiology, Brain/Liver Interface Medicine Research Center, Graduate School of Medical Sciences
[4]Mathematical Neuroscience Unit, Institute for Frontier Science Initiative
Kanazawa University, Kanazawa 920-8640, Japan
[5]CREST
[6]PRESTO
Japan Science and Technology Agency (JST), Saitama 332-0012, Japan
[7]Graduate School of Biostudies, Kyoto University, Kyoto 606-8501, Japan
*Correspondence: imai@cdb.riken.jp
http://dx.doi.org/10.1016/j.celrep.2016.02.057

SUMMARY

Super-resolution imaging deep inside tissues has been challenging, as it is extremely sensitive to light scattering and spherical aberrations. Here, we report an optimized optical clearing agent for high-resolution fluorescence imaging (SeeDB2). SeeDB2 matches the refractive indices of fixed tissues to that of immersion oil (1.518), thus minimizing both light scattering and spherical aberrations. During the clearing process, fine morphology and fluorescent proteins were highly preserved. SeeDB2 enabled super-resolution microscopy of various tissue samples up to a depth of >100 μm, an order of magnitude deeper than previously possible under standard mounting conditions. Using this approach, we demonstrate accumulation of inhibitory synapses on spine heads in NMDA-receptor-deficient neurons. In the fly medulla, we found unexpected heterogeneity in axon bouton orientations among Mi1 neurons, a part of the motion detection circuitry. Thus, volumetric super-resolution microscopy of cleared tissues is a powerful strategy in connectomic studies at synaptic levels.

INTRODUCTION

Fluorescence microscopy is a powerful approach to our understanding of three-dimensional structures in organisms. For example, antibody staining and fluorescent protein tags are often used to localize intracellular proteins in cells. In the field of neuroscience, fluorescent proteins are often used to label genetically defined neuronal circuitry using transgenic animals or to trace neurons originating from a specific area of the brain by using viral vectors. To facilitate the three-dimensional imaging of large tissues, new optical clearing techniques compatible with fluorescent proteins have been developed in recent years (Richardson and Lichtman, 2015). For example, Sca*l*e and its variant CUBIC reduce the light scattering within samples by simple soaking (Hama et al., 2011, 2015; Susaki et al., 2014). CLARITY and its variants are based on acrylamide gel hybridization, lipid removal, and index matching (Chung et al., 2013; Tomer et al., 2014; Yang et al., 2014). Both CUBIC and CLARITY actively remove scatterers (mainly lipids) to achieve excellent transparency; however, due to the harsh treatment and transient sample swelling, they can affect fine cellular morphology. Therefore, these techniques are more suitable for large-scale imaging at relatively low resolution (i.e., light-sheet microscopy at a cellular resolution).

To minimize deformation artifacts during the clearing process, we have previously developed a fructose-based optical clearing agent, SeeDB (see deep brain), which reduces light scattering without removing any components of tissues (Ke et al., 2013; Ke and Imai, 2014). SeeDB can quickly clear samples (3 days) and is compatible with various fluorescent proteins and chemical dyes including lipophilic dyes. Due to minimal changes in sample size and no loss of cellular materials, sub-micrometer-scale neuronal morphology was well preserved in SeeDB.

However, in conventional light microscopy, the lateral and axial resolution has been limited to 200–250 nm and 500–800 nm, respectively, due to the diffraction barrier (Schermelleh et al., 2010). This resolution is not sufficient to visualize fine structures of neurons, such as dendritic spines (<2 μm), axons (0.1–10 μm), and synapses (20–200 nm), and intracellular machinery, such as cytoskeletons and organelles (25–500 nm; Sigrist and Sabatini, 2012; Tønnesen and Nägerl, 2013). Therefore, electron microscopy (EM) has been utilized to obtain high-resolution structures (Kleinfeld et al., 2011; Lichtman and Denk, 2011). Especially for synaptic-scale connectomics, EM has been the only reliable method. However, despite recent technical advances, reconstruction of three-dimensional structures from serial EM images is difficult and laborious.

During the last 2 decades, various types of super-resolution (SR) fluorescence microscopy have been developed to overcome the classical diffraction limit (Schermelleh et al., 2010). For example, stimulated emission depletion (STED) microscopy and photoactivation localization microscopy (PALM) provided a diffraction-unlimited resolution (20–50 nm). Structured illumination microscopy (SIM) and newly commercialized systems based on confocal microscopy (e.g., Airyscan) extended the diffraction-limited resolution down to 100–150 nm. These are together called super-resolution microscopies. Compared to EM, super-resolution microscopy can provide rich chemical and genetic information combined with antibody staining and fluorescent proteins. However, super-resolution microscopy has a serious limitation for broader usage; because it is extremely sensitive to light scattering and spherical aberrations, sub-diffraction resolution can only be obtained at the surface of the specimens (typically up to a few micrometers in depth with oil-immersion lenses and standard mounting conditions), far below the size of cells (10–20 μm) and neuronal circuits (at least 100 μm).

To achieve super-resolution imaging of thick tissues, we tried to minimize the (1) light scattering and (2) spherical aberrations using an optical clearing and index matching strategy. In addition, during the clearing process, (3) fine structures have to be maintained, as we are unable to determine genuine fine structures from deformed samples. Because we need to obtain photons from smaller volumes than in conventional fluorescence imaging, (4) fluorophores have to be bright and stable in the cleared samples. In the present study, we used iohexol solutions to establish SeeDB2, which are optimized in all the four criteria to achieve high-resolution fluorescence imaging of thick tissues. A combination of SeeDB2 and volumetric super-resolution microscopy enabled light-microscopy-based connectomics at the synaptic scale, with rich genetic and chemical information.

RESULTS

A Quick and Efficient Optical Clearing Using a Non-ionic X-Ray Contrast Medium

To obtain high-resolution images deep inside tissues, we need to minimize both light scattering and spherical aberrations (Figure S1A). Previous efforts by our group and others have indicated that optimal refractive index (RI) of the clearing agents is 1.45–1.55 (Ke et al., 2013). To minimize spherical aberrations, the refractive indices (RIs) of samples and immersion media should be the same. Because the minimal distance between theoretically resolvable points (d) decreases as NA ($n \sin\alpha$; α is for the half opening angle of the objective) increases ($d = 0.61\lambda/NA$; according to the Rayleigh criterion) and achievable NA increases as RI of immersion media (n) increases, objective lenses for high-resolution imaging are typically designed for oil-immersion (RI 1.518). Immersion oil is also designed to match the RI of glass coverslips (RI ~1.52). Thus, the ideal optical clearing agent for high-resolution imaging should have RI 1.518. Previously, 97% 2,2′-thiodiethanol (TDE) of an RI of 1.515 has been used as a mounting medium for this purpose; however, utility of TDE has been limited, because it quenches most fluorescent proteins and some of commonly used chemical dyes (Staudt et al., 2007). Previous aqueous clearing agents, such as SeeDB (RI 1.49), could not reach this RI due to limited solubility of fructose (Ke et al., 2013). Commonly used mounting media with glycerol (RI 1.47) also cannot achieve this RI. Commercialized high-RI mounting media (e.g., CFM3 and DPX) cause shrinkage and/or have quenching issues. Therefore, large-scale volumetric super-resolution imaging has been a long-standing challenge. During our screen for high-index water-soluble agents, we noted that iodide-containing chemicals have high RI, but ionic ones are not suitable for tissue clearing (Ke et al., 2013). We then focused on non-ionic triiodobenzene compounds, such as iohexol, iopamidol, ioversol, and iodixanol, which have been originally developed as X-ray contrast media for computer-tomography imaging of human patients (Figure S1B). We found, for example, that 70.4% w/w iohexol in water reaches RI 1.518 (Figure S1C). Therefore, we tried to achieve the SeeDB concept (a simple soaking-based and morphology-preserving optical clearing agent), using high concentrations of iohexol solutions.

Iohexol solution (commercialized as Omnipaque 350; RI 1.46) has previously been reported to improve transparency of thin cornea samples (Maurice, 1987). However, iohexol alone could not efficiently clear thick brain samples by simple soaking and instead caused shrinkage of samples. This was likely because the iohexol solution did not efficiently penetrate into tissues. We therefore tested its clearing performance in combination with various detergents at 0.5%–2% and found that 2% saponin, known as a weak non-ionic detergent, can most efficiently facilitate optical clearing by iohexol without introducing morphological damages (Figures 1A, 1B, S1F, and S1G). Recently, iohexol solution (RI 1.46) with Tween-20 (named RIMS) was used to mount CLARITY samples (Yang et al., 2014); however, Tween-20 did not facilitate tissue clearing by iohexol in the simple soaking protocol. SDS and Triton X-100 at 2% caused sample deformation and/or quenching/loss of fluorescent proteins. We also tested various buffers to maintain transparency of brain samples, because brain samples soaked in non-buffered iohexol solution gradually returned opaque by unknown reasons. We found that low concentrations of Tris-EDTA buffer can maintain excellent transparency of samples when combined with iohexol (Figure S1H). In our optimized clearing protocol, tissue samples were serially incubated in lower to higher concentrations of iohexol in 2% saponin and Tris-EDTA buffer and finally equilibrated in 70.4% w/w iohexol solution in Tris-EDTA buffer (RI 1.518), named SeeDB2S (S for super-resolution; Figure 1C). For glycerol-immersion objective lenses, we also formulated a protocol to equilibrate samples at RI 1.46 (56.2% w/w or 75.5% w/v iohexol solution; named SeeDB2G; G for glycerol-immersion lens). Due to lower viscosity, SeeDB2G was useful for large tissue samples, though not best for high-resolution imaging using oil-immersion lenses. Transmission curves of cerebral cortex samples demonstrate that SeeDB2S and SeeDB2G clear brain samples better than SeeDB and RIMS (Figure 1B). Even nasal bone was well cleared with SeeDB2S (Figure 1C). Total incubation time required was a few hours (for relatively thin samples) to 2 days (adult half brain samples; Figure 1D). Like SeeDB, SeeDB2 is non-hazardous and did not introduce any fragility to tissues.

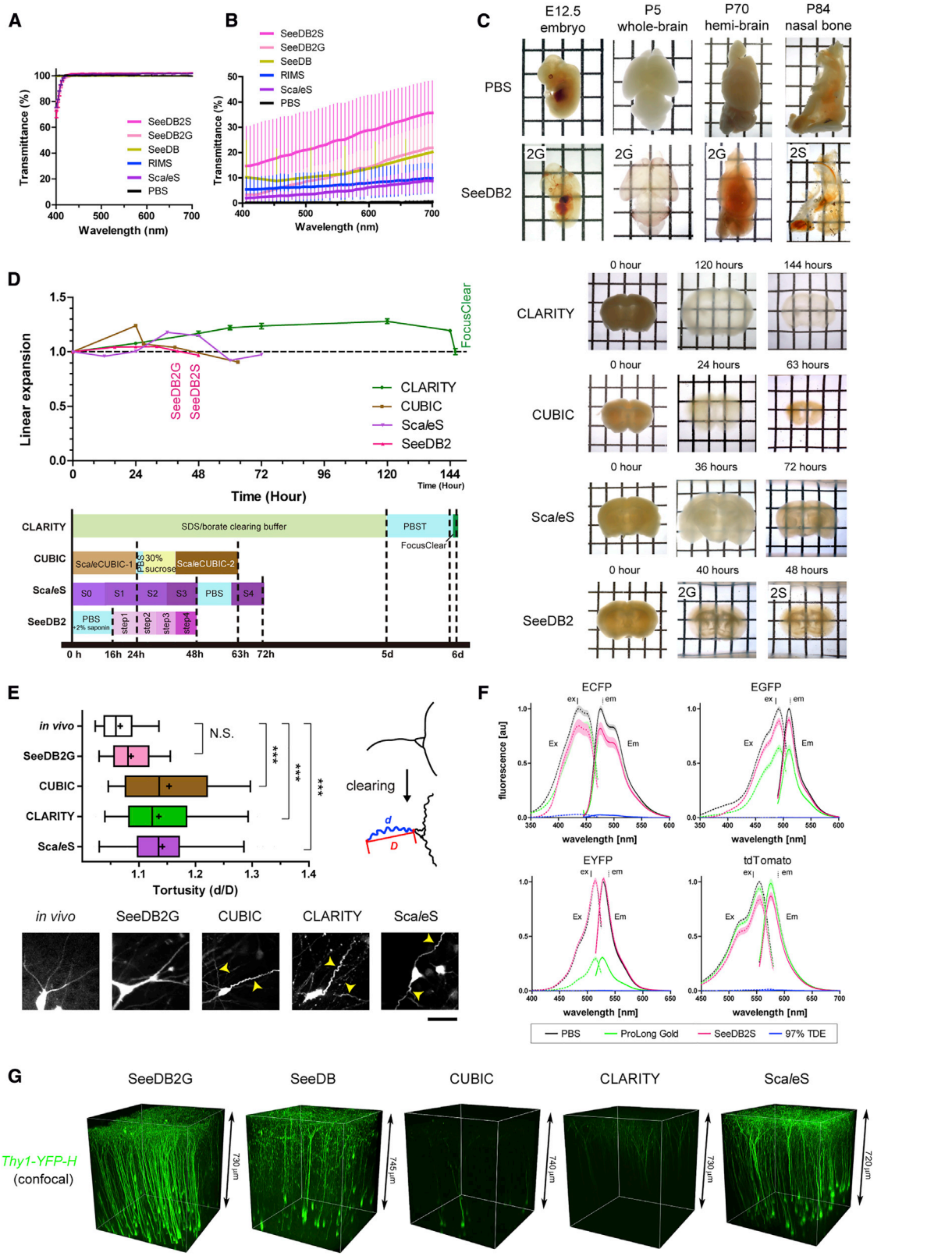

(legend on next page)

SeeDB2 Maintains Fine Neuronal Morphology

To obtain genuine high-resolution images, it is crucial to maintain fine cellular structures of samples during clearing process. This is not always well considered in other clearing protocols (Ke et al., 2013). Even recently developed clearing methods, CLARITY, CUBIC, and Sca*l*eS, are accompanied by transient sample swelling, although the final sizes of these samples were comparable to the original sample (Chung et al., 2013; Hama et al., 2015; Susaki et al., 2014). In contrast, in our SeeDB2G/S protocols, like in previous SeeDB protocol, sample sizes were maintained during the entire clearing process (Figure 1D).

To evaluate fine morphological changes during clearing, we quantified the tortuosity of smooth mitral cell dendrites in the mouse olfactory bulb, a sensitive method for this purpose (Ke et al., 2013). After clearing with CLARITY, CUBIC, or Sca*l*eS, dendrite tortuosity increased compared to in vivo, showing morphological deformation (Figure 1E). This is no surprise, given that high-order protein structures, such as cytoskeletons, do not swell and shrink isotopically. In contrast, samples cleared with SeeDB2 did not show any evidence of deformation.

SeeDB2 Preserves More Fluorescence with Lower Autofluorescence Signals

In high-resolution fluorescence imaging, we need to obtain photons from smaller volumes per pixel than in low-resolution imaging, indicating that fluorophores have to be bright and stable. We therefore examined the stability of various fluorophores in SeeDB2 and existing mounting media. Four fluorescent proteins, ECFP, EGFP, EYFP, and tdTomato, were found to be stable and showed similar excitation and emission spectra in SeeDB2 compared to those in PBS (Figure 1F). Furthermore, fluorescence signals were quite stable during long-term storage ($\geq$1 month) in SeeDB2 without accumulation of autofluorescence signals (Figures S2A–S2D). In contrast, they were dramatically quenched in 97% TDE, as has been reported previously (Staudt et al., 2007). A common commercial mounting media, ProLong Gold also reduced fluorescence of EYFP substantially. Three chemical fluorophores, Alexa 488, Alexa Fluor 555, and Alexa Fluor 647 were also found to be stable in SeeDB2S, although 97% TDE reduced fluorescence of Alexa 488 considerably (Figure S2E).

In the confocal imaging of *Thy1-YFP-H* mouse brains (Feng et al., 2000), fine dendritic tufts extending from layer 5 (L5) pyramidal neurons were better visualized in SeeDB2 than in SeeDB, CUBIC, and CLARITY, due to high fluorescence levels and low autofluorescence signals (Figures 1G, S2A, and S2C). Light-sheet microscopy enabled fast and large-scale imaging of the cerebral cortex (Figure S3A; Movie S1). SeeDB2 was also powerful for other types of samples, such as a whole embryo (E9.5) carrying the *R26-H2B-EGFP* knockin allele, in which H2B-EGFP is ubiquitously expressed at very low level (Figures S3B and S3D; Abe et al., 2011). SeeDB2 could also be used for samples stained with nuclear stains and antibodies (Figures S3E–S3G).

Resolution and Brightness Is Maintained throughout Depths in SeeDB2S

To evaluate performance of SeeDB2S in high-resolution fluorescence imaging, we first used confocal microscopy with oil-immersion lens (NA 1.40; working distance [WD] 0.13 mm) in order to quantify spatial resolution by point-spread-function (PSF) analysis of fluorescent microspheres (100 nm diameter) embedded in agarose gels. As expected, high resolution was maintained throughout depths when mounted in the index-optimized SeeDB2S (Figures 2A and 2B). However, in other mounting media with lower RI, resolution was worse, due to spherical aberrations. Axial resolution was more severely affected by the RI mismatch. To evaluate depth-dependent changes in fluorescence brightness, we performed confocal axial scans of Rhodamine 6G dye solutions from the interface of the glass coverslip (sea response; Hell et al., 1993). With SeeDB2S, the fluorescence level was maintained throughout all depths. However, in non-optimized mounting media, the brightness gradually reduced as depth increased, due to spherical aberrations (Figure 2C).

Using conventional confocal microscopy and high-NA oil immersion objective lenses, we could obtain high-resolution images of SeeDB2S-treated mouse brain slices up to the WD of objective lenses (Figures 2D and 2E). For example, we obtained high-resolution confocal images of hippocampal CA1 region in *Thy1-YFP-H* mouse brain slices cleared with SeeDB2S and then reconstructed dendrites of individual pyramidal neurons in 3D (Figure 2F). For thicker samples, the combination of

Figure 1. Fine Morphology and Fluorophores Are Preserved in SeeDB2

(A) Transmission curves of various clearing media in the visual wavelength range.

(B) Transmission curves of cerebral cortices of the mouse brains (age, postnatal day [P] 21–24; n = 3–6 each) cleared with various clearing protocols. Representative transmission images are shown on the right. Full-scan data including IR range are shown in Figures S1D and S1E.

(C) Various tissue samples before and after optical clearing with SeeDB2. A mouse embryo (E12.5), a whole brain (P5), a hemi-brain (P70), and a nasal bone (P84) before and after optical clearing with SeeDB2 are shown.

(D) Schedules of clearing and sample size changes during optical clearing by CLARITY, CUBIC, Sca*l*eS, and SeeDB2. Adult mouse brain slices (P49–56; 1.5 mm thick; n = 3 each) were used, as shown on the right.

(E) Deformation of fine neuronal structures. Tortuosity of mitral cell lateral dendritic segments were quantified and shown by box plots (n = 43, 81, 68, 58, and 80 from three to five animals). Distorted dendrites are indicated by arrowheads. Bars indicate 5th and 95th percentiles. ***$p < 0.001$ (Kruskal-Wallis test). N.S., non-significant. Scale bar represents 50 μm.

(F) Fluorescence excitation (Ex, broken lines) and emission (Em, solid lines) spectra of fluorescent proteins in various clearing media. Fluorescence levels were normalized to the maximum intensity in PBS. Excitation (ex) and emission (em) wavelength for Em and Ex curves, respectively, are indicated on the top. n = 3 each.

(G) Confocal imaging of *Thy1-YFP-H* mouse (P72–84) cerebral cortex after various optical clearing methods (representative images out of four each). Images were taken from the surface of the hemi-brain samples under the same imaging conditions using a 20× air objective lens. Grids in transmission images are 2.6 × 3.2 mm.

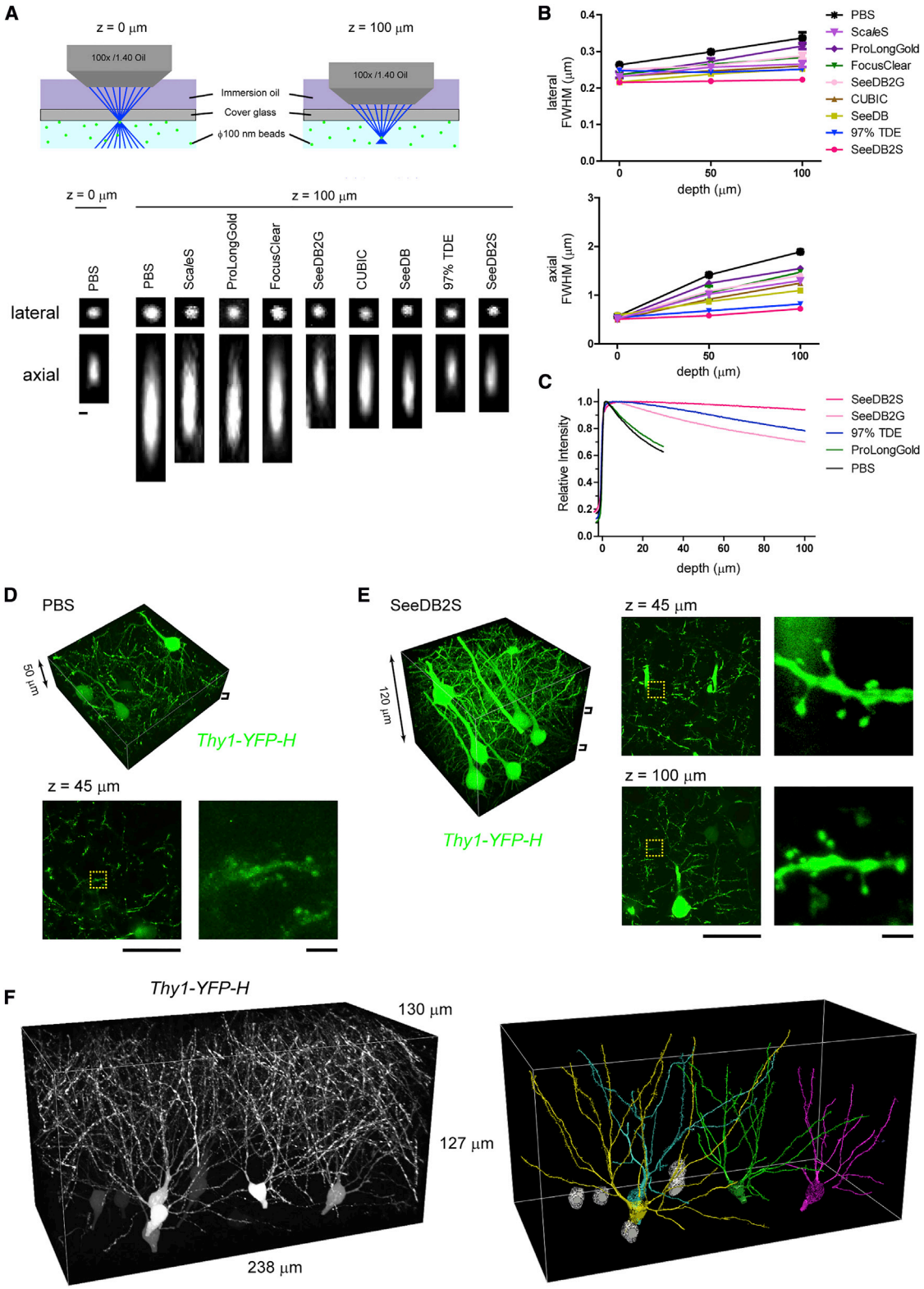

Figure 2. Resolution and Brightness Are Consistent throughout Depths in SeeDB2S

(A) Point-spread-function (PSF) analysis of fluorescent microspheres (diameter, 100 nm) in various clearing and mounting media. Fluorescence images of the microspheres obtained with confocal microscopy (pinhole size, 1AU) and an oil-immersion objective lens (100×; NA 1.40; WD 0.13 mm) are shown.

(legend continued on next page)

SeeDB2G and high-NA glycerol-immersion lens with longer WD (NA 1.30; WD 0.30 mm) was useful; we could obtain high-resolution images of olfactory axons converging to a glomerulus in the olfactory bulb (Figure S3C).

Deep-Tissue Super-Resolution Microscopy Using SeeDB2S

We next evaluated the performance of SeeDB2S in super-resolution microscopy. We tested a commercialized STED microscope with an oil-immersion objective lens (NA 1.40; WD 0.13 mm). To determine the lateral PSF at various depths, we used 40-nm-diameter fluorescence microspheres embedded in agarose. In SeeDB2S and 97% TDE, 50–60 nm full width at half maximum (FWHM) in *x-y* was maintained up to 100 μm depth; however, in ProLong Gold and PBS, resolution was quickly degraded (Figure 3A).

We next imaged *Thy1-YFP-H* mouse brain slices cleared with SeeDB2S under the same STED laser conditions. We could obtain sub-diffraction images up to ~120 μm in depth, the upper limit set by the WD of an objective lens (Figure 4B). We could visualize the fine geometry of dendritic spine heads and spine necks, which are essential information to understand synaptic functions (Figure 3C). In addition, we occasionally observed filopodia extending from existing spine heads, which is difficult to resolve using conventional microscopy (Figure 3C). To evaluate resolutions at various depths in brain tissues, we determined spine neck diameters, which are known to be thinner than the diffraction limit (Tønnesen et al., 2014). We found no difference in spine neck diameters quantified at superficial (~30 μm) and deep areas of brain slices (~110 μm; Figure 3D). Thus, SeeDB2S enables STED microscopy an order of magnitude deeper than previously possible under standard mounting conditions. It should be noted that deep-tissue STED microscopy has only been achieved by two-photon excitation STED (Ding et al., 2009; Moneron and Hell, 2009) or by manual optical calibration (Urban et al., 2011); for the latter, it is currently unrealistic to manually correct the RI mismatch at each *z* position in order to obtain large-scale 3D images.

Volumetric Super-Resolution Imaging for Cell Biology

A different type of super-resolution microscopy, SIM allows multi-color imaging and has often been used for cell biology applications. Here, we used a commercial SR-SIM system with an oil-immersion lens (NA 1.46; WD 0.11 mm) to image SeeDB2S samples. HEK293T cells (~10 μm thick) labeled with membrane EGFP, MitoTracker, and DAPI could be fully resolved with 3D SR-SIM in SeeDB2S, but not in PBS. For example, fine filopodia extending from the plasma membrane were better resolved in SeeDB2S (Figure 3E).

Mouse oocytes are even more challenging for high-resolution imaging, due to its large size (~80 μm in diameter; Kitajima et al., 2011). Therefore, it has been difficult to resolve individual microtubules using existing confocal microscope systems (Figure 3F). Using a commercial super-resolution system, FV-OSR, with an oil-immersion lens (NA 1.40; WD 0.13 mm), we could resolve individual microtubules of oocytes during meiosis I (Figure 3F; Movie S2).

Volumetric Super-Resolution Imaging for Connectomics

Large-scale super-resolution imaging may be particularly powerful for connectomics applications combined with fluorescent proteins. Here, we used a commercial super-resolution microscopy, Airyscan, which is based on multi-array GaAsP detectors and pixel reassignment (Huff, 2015). Due to the relatively high photon budget and low photo-bleaching among various super-resolution microscopies, Airyscan was useful for large-scale imaging, although the resolution was not as good as STED. In PSF analysis, the high resolution (~150 nm in *xy*; ~360 nm in *z*) was maintained throughout depth using an oil-immersion lens (NA 1.40; WD 0.19 mm; Figure 4A).

We compared images of the same region of a *Thy1-YFP-H* mouse brain slice, using two-photon microscopy, confocal microscopy, and Airyscan. Because the longer excitation wavelength is the lower resolution becomes ($d = 0.61\lambda/NA$), two photon microscopy is not good for high-resolution imaging. Airyscan best resolved dense neuronal circuits labeled with EYFP (Figure 4B). Filopodia and thin spines, often missed in two-photon microscopy, were reliably identified with Airyscan. We could also obtain large-scale super-resolution images with SD-OSR (Hayashi and Okada, 2015) and SP8-HyVolution (Figures S4B–S4D).

Due to excellent axial resolution, dendritic spines extending along z axis could be reliably detected with SeeDB2S up to >100 μm depth, but not with other mounting media, due to spherical aberrations (Figure 4C; Movie S3). In the corpus callosum, L2/3 callosal axons densely labeled by in utero electroporation were well resolved in SeeDB2S, but not in Sca*l*eS (Figure 4D). Improvement of axial resolution in SeeDB2S is particularly important in circuit tracing, as it becomes easier to dissect crossing over of multiple fibers along z axis. In the axon bundles of olfactory sensory neurons, unmyelinated thin axonal fibers (200–300 nm in diameter, consistent with earlier EM studies) labeled with *MOR29B-IRES-EYFP* transgene were

(B) Full width at half maximum (FWHM) for lateral and axial directions are shown. Note that axial resolution was more severely affected by the RI mismatch. n = 20 each.

(C) Confocal axial scans of rhodamine dye solutions from the interface with the glass coverslip. Due to spherical aberrations, photons detected by PMT decrease as the depth increases when RI is mismatched. Intensity curves were normalized to the maximum intensity in each condition.

(D and E) High-resolution confocal imaging of *Thy1-YFP-H* mouse brain slices (cerebral cortex) using an oil-immersion objective lens (100×; NA 1.40; WD 0.13 mm). Representative images in PBS (D) and SeeDB2S (E) are shown.

(F) Hippocampal CA1 region (238 μm × 127 μm × 130 μm) of a *Thy1-YFP-H* mouse brain slice was imaged using a 100× oil-immersion objective lens (NA 1.40; WD 0.13 mm). Both lateral and axial resolution was sufficiently high to trace individual EYFP-labeled neurons. Reconstructions of four pyramidal neurons are shown on the right. Using semi-automated tracing software, Neurolucida, we could obtain near-complete wiring patterns from this densely labeled brain slice. Mice were P48–56.

Scale bars represent 200 nm in (A), 50 μm in (D, left) and (E, left), and 2 μm in (D, right) and (E, right).

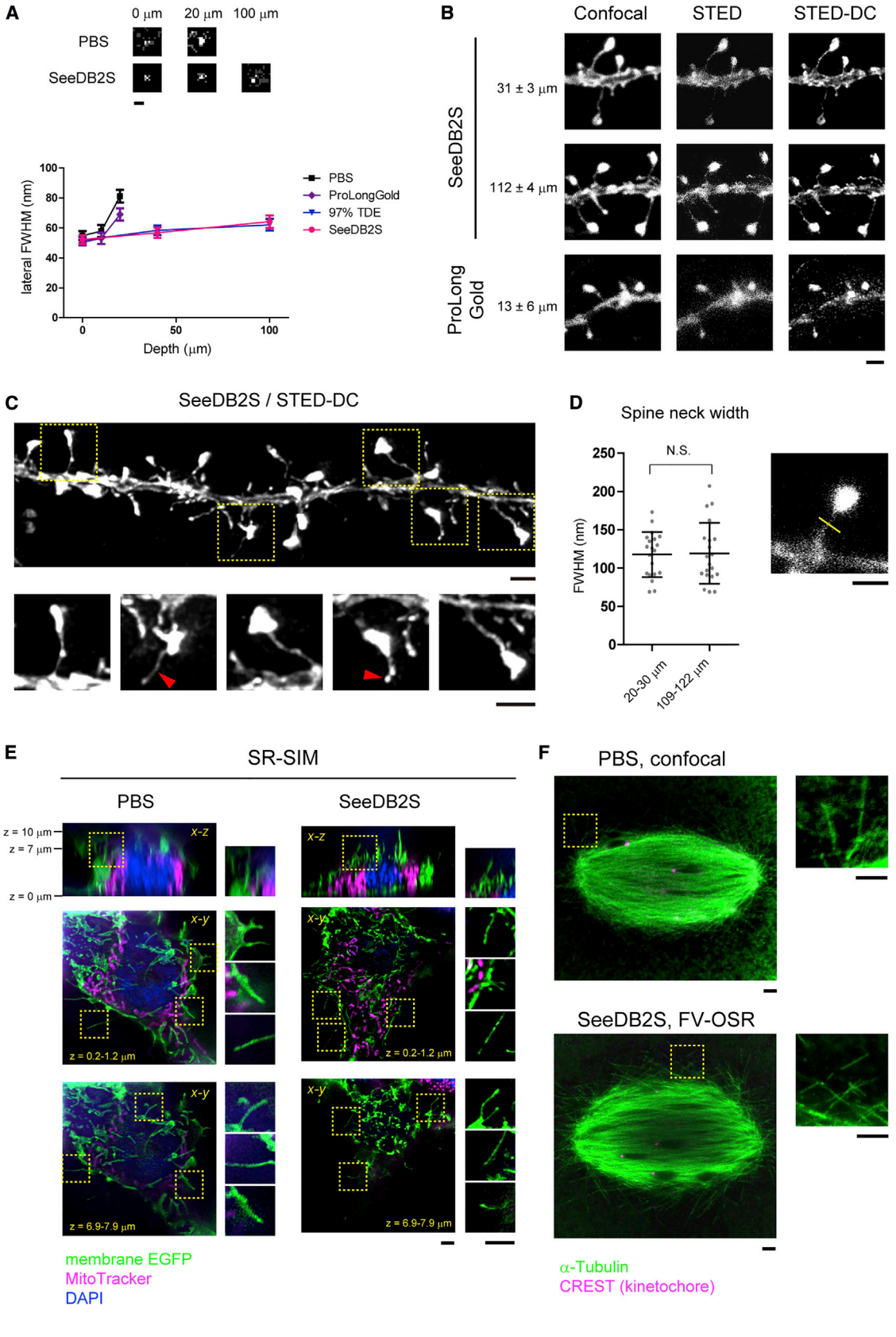

(legend on next page)

well resolved and dissected in SeeDB2S (Figure 4E; see also Figure S4D for multi-color imaging). In the large-scale super-resolution images of the cerebral cortex (100 μm thick; adult *Thy1-YFP-H* mouse), we could reliably identify dendritic spines and axonal boutons at all depth (Figure 5A; Movie S4) and reconstruct them in 3D (Figure 5B; Movie S5). Thus, the combination of SeeDB2S and super-resolution microscopy is useful for large-scale synapse mapping.

Comprehensive Synapse Mapping in Dendrites of NMDA-Receptor-Deficient Neurons

Many cognitive and mental disorders are caused by synaptic abnormalities, and thus, the super-resolution mapping of synapses can become a powerful tool for our understanding of learning-related synaptic changes and their pathology. Using Airyscan, we mapped excitatory and inhibitory synapses in wild-type and NMDA-receptor-deficient L5 pyramidal neurons, in which an essential NR1 subunit was knocked out using in utero electroporation (Figures 6A and 6B; Tsien et al., 1996). Excitatory synapses are known to localize at the tip of mature dendritic spines in L5 neurons, and their size is correlated with the spine head diameter. Based on spine head diameter, we classified dendritic spines into three types: filopodia (<250 nm), thin spine (250–500 nm), and mushroom spine (>500 nm; Figure 6C). To visualize post-synaptic structures of inhibitory synapses, we used EYFP-gephyrin (Chen et al., 2012). EYFP-gephyrin puncta were found in dendritic shaft and a subset of spine heads, and these two types were unambiguously distinguished in our super-resolution images (Figures 6A and 6B). We focused our analysis on 100–200-μm-long unbranched oblique dendrites extending from the trunk of apical dendrites, from the proximal to distal end in full, to avoid any biases in quantification.

In the NR1-deficient neurons, total spine density and average spine length were unchanged (Figures 6D and 6E), but the distribution of spine head diameters was different from wild-type (Figures 6C, 6D, and 6F). Increase in average spine head diameter is consistent with an earlier study using cortex-specific NR1 knockout mice (Ultanir et al., 2007). As for EYFP-gephyrin puncta, density in the shaft was not affected significantly; however, density in spine heads was increased in KO (Figure 6G). We also found that EYFP-gephyrin puncta tended to accumulate at large spine heads in the NR1 KO neurons (Figures 6H and 6I). Thus, the NMDA receptor knockout affects not only excitatory synapses but also inhibitory synapses directly or indirectly. Recruitment of inhibitory synapses to large spines in the NR1-deficient neurons may be due to an activity-dependent homeostatic action of inhibitory synaptogenesis in these spines (Baho and Di Cristo, 2012).

Mapping of Pre-synaptic Structures in the Fly Motion Detection Circuits

SeeDB2 is useful not only for mammalian tissues but also for insect brains. Because a fly brain is at most 300 μm thick, a commercialized high-NA and long WD objective lens (NA 1.30; WD 0.30 mm) for glycerol immersion could be used for high-resolution confocal imaging of an entire fly brain cleared with SeeDB2G. Using a *bsh-Gal4 UAS-CD8GFP* fly (Hasegawa et al., 2011), we could obtain comprehensive maps of *bsh*-positive neurons, a subset of optic lobe neurons and central brain neurons, in the whole brain (Figures 7A and 7B; Movie S6).

In the medulla, the *bsh-Gal4* line labels Mi1 neurons, which constitute a part of the light edge (ON edge) motion detection pathway (Takemura et al., 2013). From an EM-based small-scale connectomic study, it has been proposed that T4 neuron detects the motion based on inputs from Mi1 and Tm3 neurons. However, the mechanisms of the motion detection in this circuit are not fully understood (Borst and Helmstaedter, 2015). Here, we used SeeDB2S and super-resolution microscopy (Airyscan) for large-scale reconstruction of Mi1 neurons in the medulla. We noted unique hairpin-shaped and tripartite axonal bouton-like structures in Mi1 neurons, which have been difficult to resolve using conventional confocal microscopy or with a commonly used mounting media (Figures 7C–7E). Our large-scale high-resolution quantification revealed that the tripartite axonal boutons oriented to various directions relative to the axonal shaft, whereas dendrites in M1 and M5 layers were consistently extended anteriorly (Figures 7F and 7G). It has been reported that four different types of T4 neurons with different direction selectivity show distinct dendritic orientations in M10 layer (Maisak et al., 2013; Takemura et al., 2013). Thus, various orientations of Mi1 axonal

Figure 3. Deep-Tissue Super-Resolution Imaging Using SeeDB2S

(A) PSF analysis of fluorescent microspheres (diameter, 40 nm) in various mounting media was determined using STED microscopy with an oil-immersion lens (100×; NA 1.40; WD 0.13 mm). Lateral FWHM obtained with 2D STED is shown. n = 20 each.

(B) STED microscopy of the *Thy1-YFP-H* mouse brain slices cleared with SeeDB2S. Dendritic spines of cortical pyramidal neurons are shown (z-stacked images). Confocal and STED images are compared. STED images were further deconvoluted (DC) on the right. Fine spine geometry was fully resolved using STED microscopy up to ~100 μm depth in SeeDB2S. In contrast, super-resolution images could not be obtained with ProLong Gold even at ~10 μm depth.

(C) Representative STED images cortical pyramidal neurons (~60 μm depth). Red arrowheads indicate filopodia extending from spine heads.

(D) To evaluate resolution of STED microscopy at surface (20–30 μm) and deep (109–122 μm) areas, we quantified spine neck diameter, which is known to be below the diffraction limit. A lateral FWHM of spine neck diameter was comparable between two depths (~120 nm; data are mean ± SD; N.S., non-significant in two-tailed Welch's test; n = 20 each), suggesting consistent resolution of the STED microscopy. Mice were P56–64.

(E) HEK293T cells expressing membrane EGFP were stained with DAPI (nuclei) and MitoTracker (mitochondria) and imaged using 3D SR-SIM. Optical *x-z* or *x-y* sections (1-μm stacked images) are shown. Because axial scales are expanded in PBS samples with RI 1.33, calibrated depths are shown in the figures. Note that fine filopodia extending from the plasma membrane were better resolved in samples cleared with SeeDB2S than in PBS. SR-SIM images of mouse brain slices are shown in Figure S4A.

(F) Mouse oocytes during meiosis I were labeled with anti-tubulin and CREST (anti-kinetochore) antibodies and imaged with a confocal microscope. A water-immersion objective lens (40×; NA 1.20; WD 0.28 mm) was used for the PBS sample. In FV-OSR super-resolution system, an oil-immersion objective lens (100×; NA 1.40; WD 0.13 mm) was used to image the SeeDB2S-cleared sample. Note that microtubules were better resolved in samples cleared with SeeDB2S and imaged using FV-OSR.

See also Movie S2. Scale bars represent 100 nm in (A), 1 μm in (B)–(D), 2 μm in (E), and 5 μm in (F).

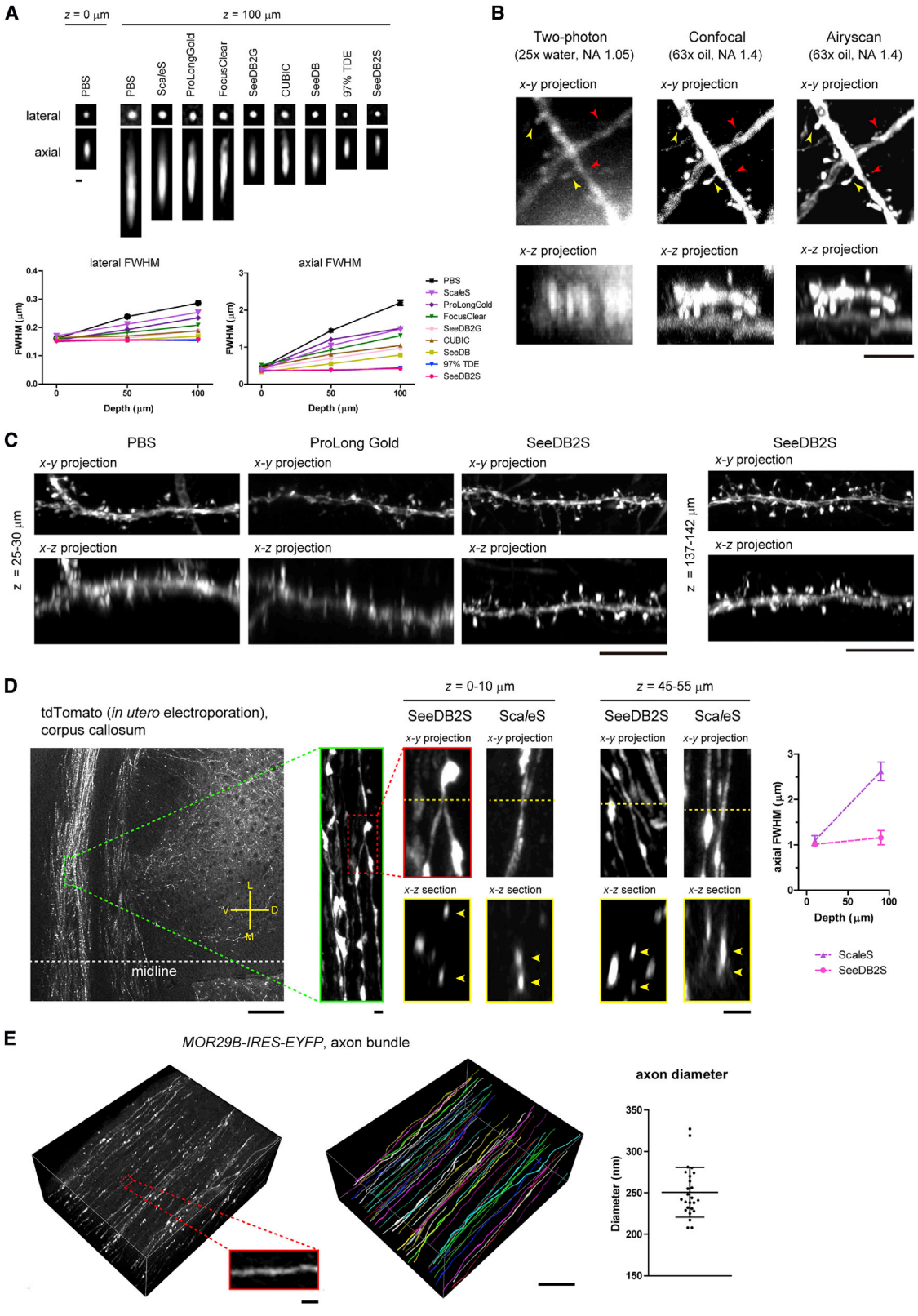

(legend on next page)

boutons may indicate specific connectivity of each Mi1 type to a particular subtype of T4 neurons, particular dendritic compartments of post-synaptic neurons, and/or spatial displacement of Mi1 outputs, all of which are excellent candidates for the origin of motion detection (Borst and Helmstaedter, 2015; Shinomiya et al., 2014; Figure 7H).

DISCUSSION

Clearing Methods for Large-Scale versus High-Resolution Imaging

Previously, most of tissue-clearing techniques have been aimed to achieve 3D imaging of large tissues (e.g., whole brain) by reducing light scattering. However, light scattering is also a major obstacle for high-resolution imaging. In the present study, we aimed to establish an optimized clearing agent for super-resolution 3D imaging. In our SeeDB2S, we tried to minimize not only light scattering but also spherical aberrations, another big problem for high-resolution imaging (Figure S1A). We also tried to maximally preserve fine morphology and fluorophore brightness during clearing, essential factors in super-resolution imaging. Because quantitative parameters are no longer preserved in the deformed samples, imaging of intact structure with SeeDB2S is a big advantage over other clearing techniques accompanying transient swelling (e.g., CLARITY, CUBIC, and Sca*l*eS) and a new type of super-resolution microscopy, expansion microscopy, based on physical expansion of samples (Chen et al., 2015). SeeDB2S was useful not only for brain tissues but also for more fragile samples for cell biology, such as cultured cells and mouse oocyte, maintaining fine structures of microtubules, actin fibers, mitochondria, and plasma membranes (Figures 3E, 3F, S4F, and S4G). SeeDB still has advantages in particular applications; because SeeDB is detergent-free, ultrastructures including plasma membrane were well preserved in the EM (Y. Fukazawa, personal communication). Because even small amount of detergent has deleterious effects on plasma membrane integrity, SeeDB may be the best for this purpose.

Admittedly, the transparency possible with SeeDB or SeeDB2 is not as good as those of CLARITY or CUBIC, which are aimed for whole-brain imaging (Figure 1D). However, to achieve this higher transparency, lipids have to be removed through harsh treatments. To facilitate penetration of antibodies (~10 nm size) into tissues, more damage to the nano-scale structures are inherently inevitable. Therefore, there is no one all-powerful method and there is a trade-off between the achievable transparency and the preservation of fine structures. It is important to choose the best method based on the primary factors for volumetric imaging (Richardson and Lichtman, 2015).

SeeDB2S for Volumetric Super-Resolution Imaging of Intact Tissue Structure

Using SeeDB2S, we established the deep-tissue super-resolution imaging of intact tissue samples up to 100 μm scale. We demonstrated the power of our approach for various types of super-resolution microscopy, including STED microscopy, SR-SIM, FV-OSR, SD-OSR, SP8-HyVolution, and Airyscan (Figures 4 and S4; Table S1). Among these microscopes, the highest lateral resolution (~50 nm for our samples) could be achieved with STED microscopy. Axial resolution can also be improved in 3D STED. We also confirmed that SeeDB2S is compatible with single-molecule localization-based super-resolution microscopy, such as PALM with mEos2, in cultured cells (Figures S4F and S4G). To obtain large-scale images, Airyscan was most useful due to the minimal photo-bleaching that occurs. Currently, the imaging scale is limited by the WD of oil-immersion objective lenses (currently 100–200 μm for NA $\geq$ 1.4) and scanning/processing speed of the microscopes. In the future, new lenses with longer WD should expand the imaging depth further. Ultrafast super-resolution microscopy, such as lattice light-sheet SIM, should facilitate the large-scale volumetric super-resolution imaging (Chen et al., 2014).

Light-Microscopy-Based Connectomics

Super-resolution fluorescence imaging with SeeDB2S opens the new opportunity of light-microscopy-based connectomics at single-fiber and synapse resolution (Figures 3, 4, 5, 6, and 7). Combined with commercially available super-resolution imaging systems, we could obtain fine structures of axonal boutons and dendritic spines. Previously, the single-fiber tracing has been performed using serial EM. However, these approaches have been laborious and are limited to relatively small volumes with little genetic and chemical information. A recent report on volumetric super-resolution microscopy also depends on laborious serial sectioning (Sigal et al., 2015). Now, our SeeDB2S can be used to achieve this goal with much less effort. Large-scale synapse mapping, i.e., whole-neuron scales in mammals and whole-brain scales in fly, should provide important information for our understanding of neuronal computation.

Figure 4. Improved Performance of Neuronal Tracing with SeeDB2S

(A) PSF analysis of fluorescent microspheres (diameter, 100 nm) imaged with Airyscan super-resolution microscopy. FWHM for lateral and axial directions are shown. n = 20 each.

(B) Comparison of resolution obtained with two-photon microscopy, confocal microscopy, and Airyscan microscopy (*Thy1-YFP-H*; cerebral cortex; ~P56). The "stubby" spines found in two-photon microscopy were not stubby in Airyscan (yellow arrowheads). Some spines detected in Airyscan were missing in two-photon microscopy (red arrowheads).

(C) Brain slices from adult *Thy1-YFP-H* mouse (P181) in PBS, ProLong Gold, and SeeDB2S were imaged with Airyscan super-resolution microscopy. *x-y* and *x-z* projection images of dendrites are shown. Note that axial resolution is much improved with SeeDB2S. See also Movie S3.

(D) Tracing densely labeled axons in the corpus callosum (Airyscan). Layer 2/3 pyramidal neurons were labeled with tdTomato using in utero electroporation (P56). *x-z* sections of crossing-over points are shown in yellow boxes. Axial FWHM of axon signals are mean ± SEM (n = 30–35). D, dorsal; L, lateral; M, medial; V, ventral.

(E) Tracing and quantification of axons for olfactory sensory neurons (Airyscan). Axon diameter data are mean ± SD. Dorsal olfactory epithelium and axon bundles were dissected from transgenic *MOR29B-IRES-EYFP* mice (P35) and cleared with SeeDB2S. All labeled axons were reconstructed on the right.

Scale bars represent 200 nm in (A), 5 μm in (B), 10 μm in (C), 100 μm in (D, left), 2 μm in (D, middle and right), 1 μm in (E, left), and 10 μm in (E, right).

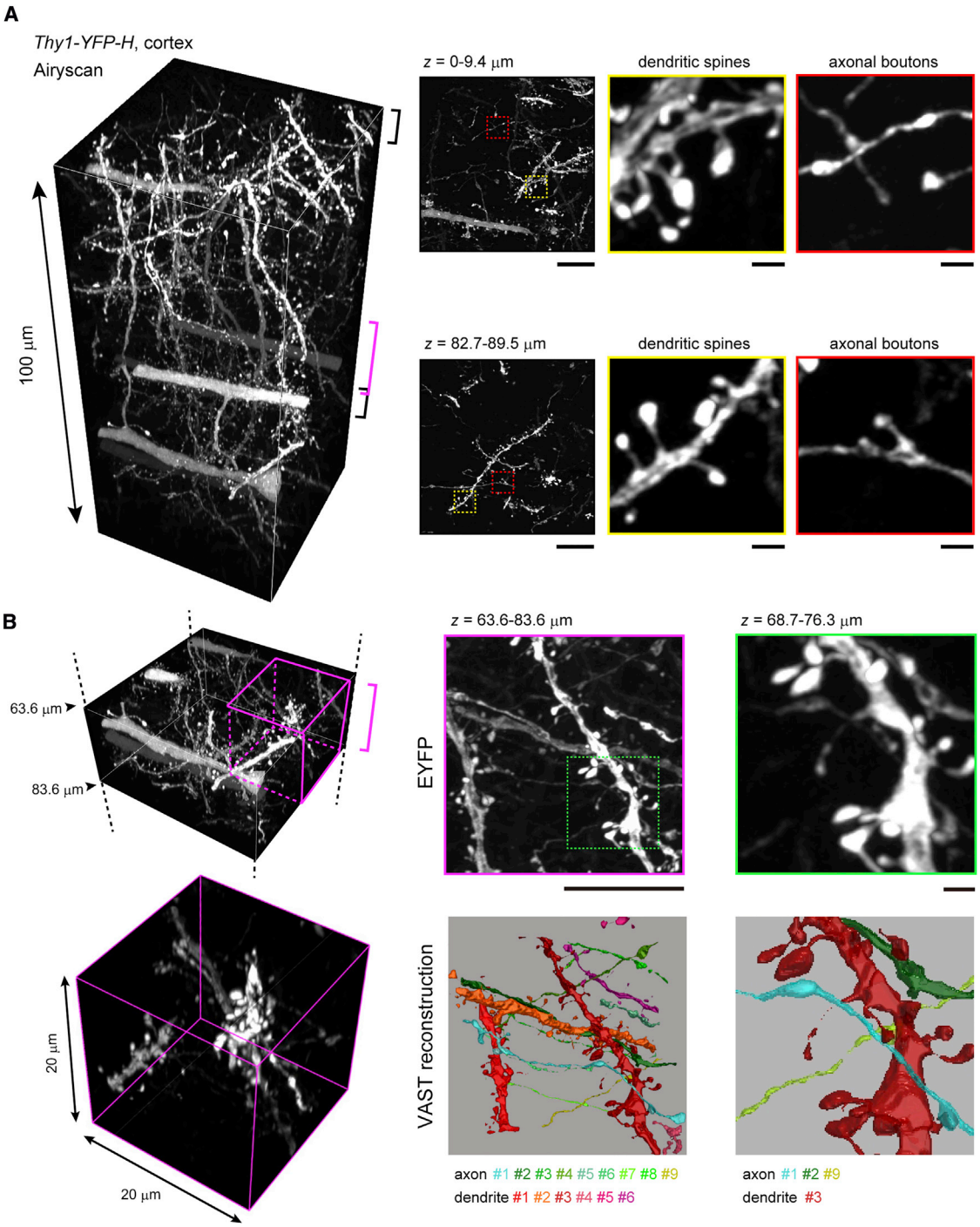

Figure 5. Large-Scale Super-Resolution Imaging of Neuronal Circuitry Cleared with SeeDB2S

(A) 3D rendering of cerebral cortex of an adult *Thy1-YFP-H* mouse (P56), imaged with Airyscan microscopy. See also Movie S4. High-magnification images are shown on the right.

(B) 3D rendering and VAST reconstruction (Kasthuri et al., 2015) for a part of (A). See also Movie S5. See Figure S5 for the image processing pipeline.

Scale bars represent 10 μm in (A, left) and (B, left) and 1 μm in (A, middle and right) and (B, right).

It should be noted that the practical lateral resolution using our approach is currently 50–150 nm and, for now, the serial EM approaches with sub-nm to 10-nm resolutions remains to be the best way for the "saturated" connectomics for all neurons in a volume (Kasthuri et al., 2015). Rather, volumetric super-resolution imaging can become a complementary approach to

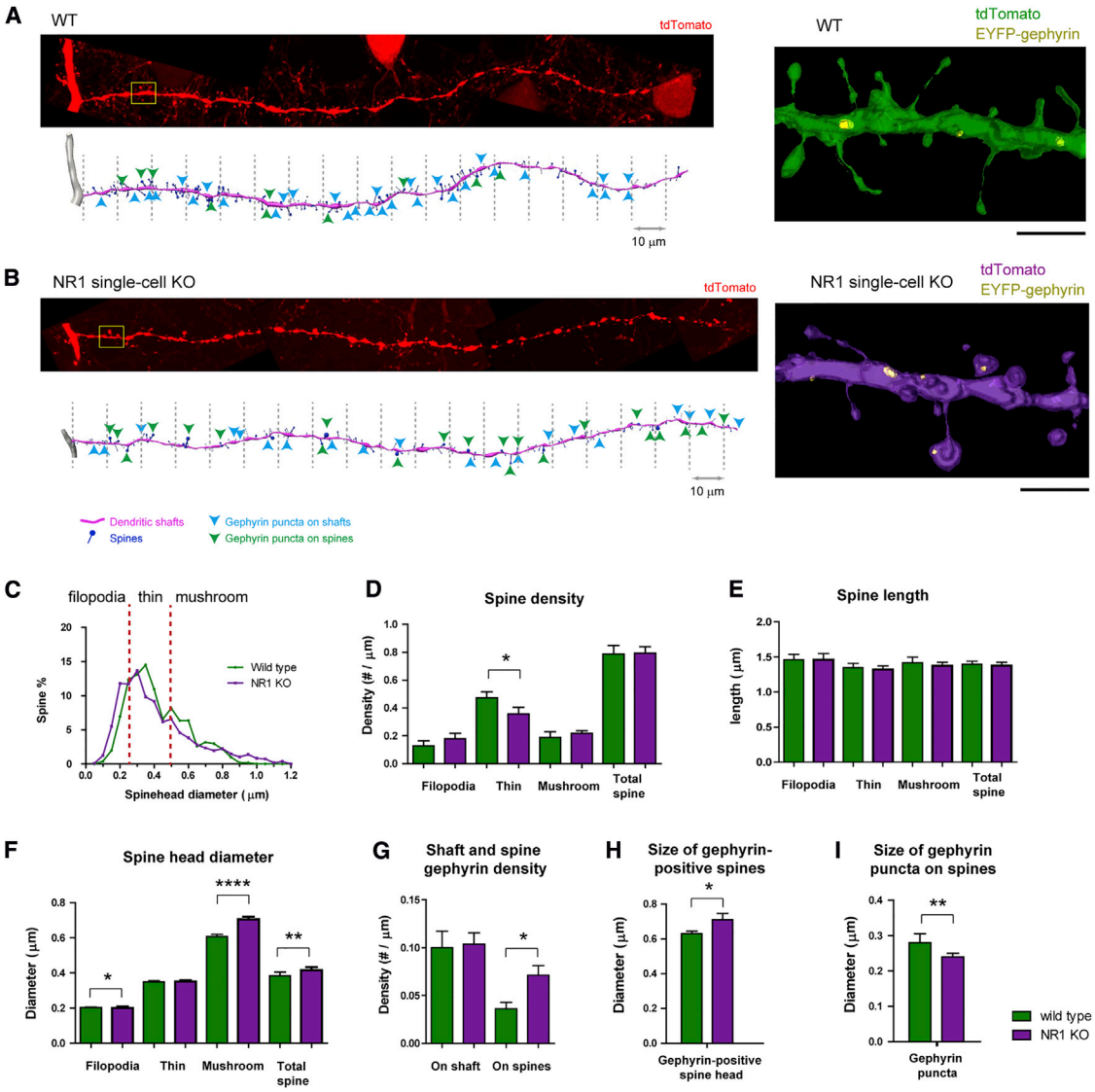

Figure 6. Quantitative Analyses of Excitatory and Inhibitory Synapses in Wild-Type and NMDAR-Deficient Neurons Using Volumetric Super-Resolution Microscopy

(A and B) L5 neurons were labeled with cytoplasmic tdTomato and EYFP-gephyrin using in utero electroporation and analyzed at P22 (Airyscan). Unbranched oblique dendrites (100–200 μm long) extending from the trunk of the proximal part of apical dendrites of L5 pyramidal neuron were analyzed. Representative super-resolution images are reconstructed with VAST. Note that gephyrin puncta on dendrite shaft versus spines are unambiguously defined. Both wild-type (A) and NR1-deficient neurons (B) were analyzed.

(C) Definition of three types of spines (filopodia, thin, and mushroom) based on spine head sizes.

(D–F) Quantifications of spine head density (D), spine length (E), and spine diameter (F) of WT and NMDAR-KO neurons.

(G) Density of EYFP-gephyrin puncta in WT and NMDAR-KO neurons.

(H) Sizes of gephyrin-positive spine heads.

(I) Size of gephyrin puncta on dendritic spines. *$p < 0.05$; **$p < 0.01$; ****$p < 0.0001$ (Mann-Whitney U test).

n = 503 and 1,068 spines in (D) and (E). n = 5 (WT) and 8 dendrites (KO) in (F) and (G). n = 22 (WT) and 97 (KO) spines in (H) and (I). Data are mean ± SEM. Scale bars represent 2 μm.

EM-based connectomics with its imaging speed, low cost, scalability, multi-color options, and compatibility with genetic and chemical labeling strategy. Sparse genetic labeling and multi-color labeling (e.g., Brainbow) should help improve the reliability in super-resolution circuit tracing (Livet et al., 2007); in fact, SeeDB2 is compatible with the multi-color labeling strategy (Figure 1F; data not shown). Genetic labeling of synaptic proteins should facilitate the accurate identification of synapses (Figure 6; Chen et al., 2012). Combined with antibody staining with synaptic proteins, volumetric super-resolution microscopy can

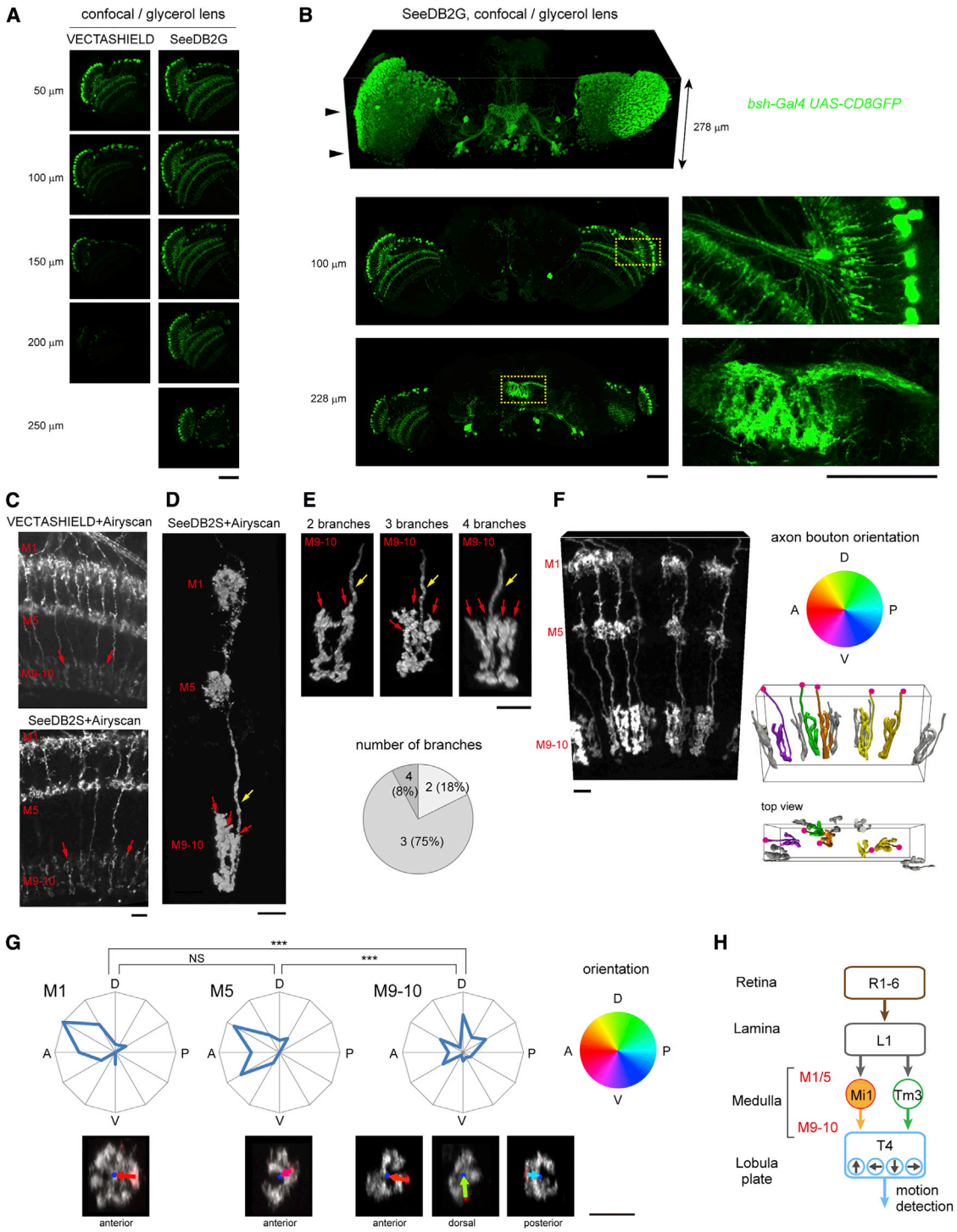

Figure 7. Dissecting a Motion Detection Circuitry in the Fly Brain

(A) SeeDB2 is useful for fluorescence imaging of the fly brain. The sequential optical sections of the optic lobes from a brain of a *bsh-Gal4 UAS-CD8GFP* fly, cleared with SeeDB2G and imaged with a glycerol-immersion objective lens with long WD (63×; NA 1.30; WD 0.30 mm). Dorsal views (anterior to the top) are shown. The left and right columns are the fly brains mounted in Vectashield and SeeDB2G, respectively. Note that the signal intensity and resolution are unaltered throughout z-sections in the latter.

(B) A 3D reconstruction and horizontal sections at 100 μm and 228 μm of the whole brain image mounted in SeeDB2G. The enlarged view of the first optic chiasm at 100 μm shows axons of the lamina neurons (L4 and L5). The fan-shaped body involved in visual memory formation was found at 228 μm. See also Movie S6.

(legend continued on next page)

become an alternative to the time-consuming array tomography (Micheva and Smith, 2007) and serial-section STORM (Sigal et al., 2015; Figure S4E). Fueled by ongoing efforts in genetic circuit labeling and automated neuronal reconstruction pipelines (Peng et al., 2015), the volumetric super-resolution microscopy should facilitate light-microscopy-based neuronal circuit reconstructions at synaptic resolutions.

EXPERIMENTAL PROCEDURES

Additional details are available in the Supplemental Experimental Procedures.

Reagents

For SeeDB2G, Omnipaque 350 (e.g., Daiichi-Sankyo; 75.5% w/v or 56.2% w/w iohexol in Tris-EDTA buffer) was used. SeeDB2S was prepared by dissolving iohexol powder (available as Histodenz from Sigma-Aldrich or Nycoden from Axis-shield) at 70.4% w/w in 10 mM Tris-Cl (pH 7.6), 0.267 mM EDTA. Note that SeeDB2S was prepared based on % w/w not w/v. Solutions 1 and 2 (see below) were prepared by diluting Omnipaque 350 in H_2O and adding saponin (Nacalai Tesque or Sigma-Aldrich) at 2% w/v. Saponin shows different levels of browning across lots (especially from Sigma-Aldrich). We therefore used lots with a less brownish color because the brown pigment reduces the light transmittance. Stock solution of saponin (20% w/v) was filter sterilized. Refractive indices were determined using an Abbe refractometer (Erma) and white light source.

Optical Clearing of Mouse Brain Tissues Using SeeDB2

All animal experiments were approved by the Institutional Animal Care and Use Committee of the RIKEN Kobe Institute. Paraformaldehyde-fixed mouse brain samples were cleared using 5 ml Eppendorf tube with gentle rotation (~4 rpm) using an overhead rotator (TAITEC) at room temperature (25°C). First, fixed tissue samples were incubated 2% saponin in PBS overnight. Samples were next incubated in 1:2 mixture of Omnipaque 350 (Daiichi-Sankyo) and H_2O with 2% saponin (solution 1) for 6–10 hr and then in 1:1 mixture of Omnipaque 350 and H_2O with 2% saponin (solution 2) for 6–10 hr. Finally, samples were incubated in Omnipaque 350 with 2% saponin (solution 3) for $\geq$12 hr. Thin brain slices could be cleared with shorter incubation schedules. Some samples (e.g., lipid-rich tissues and large samples) may be further cleared by prolonged incubation in solution 3. For clearing with SeeDB2S, samples were further incubated in SeeDB2S with 2% saponin (solution 4) for $\geq$12 hr. Cleared tissues were transferred to SeeDB2G or SeeDB2S without saponin for imaging. For long-term storage of samples, 0.01% sodium azide can be added as a preservative. The addition of antifade chemicals (e.g., DABCO) is not recommended for fluorescent protein samples, because they often quench fluorescent proteins. Samples can be stored at room temperature under protection from light. The cleared sample should not be exposed to the air for long time, because the surface may become sticky due to water evaporation. A step-by-step protocol and technical tips of SeeDB2 will be posted in our website, SeeDB resources (https://sites.google.com/site/seedbresources/).

SUPPLEMENTAL INFORMATION

Supplemental Information includes Supplemental Experimental Procedures, five figures, one table, and seven movies and can be found with this article online at http://dx.doi.org/10.1016/j.celrep.2016.02.057.

AUTHOR CONTRIBUTIONS

M.-T.K. performed most of the experiments. Y.N., R.T., and M.S. analyzed fly brain data. S.F. prepared some mouse samples. S.Y. and T.S.K. prepared mouse oocyte samples. T.I. conceived the experiments, supervised the project, and performed experiments on cultured cells and recombinant proteins. T.I. wrote the manuscript with input from all authors.

ACKNOWLEDGMENTS

We thank J.R. Sanes (*Thy1-YFP-G*, *H*), A. Tsuboi (*MOR29A/B*), S. Tonegawa (floxed *Grin1*), and the Laboratory for Animal Resources and Genetic Engineering (LARGE) at the RIKEN Center for Life Science Technologies (*R26-H2B-EGFP*) for providing mouse strains. We also thank S. Okabe and J.W. Lichtman for valuable suggestions, Y. Fukazawa for sharing unpublished results, R. Iwata for help with statistical analysis, and M.N. Leiwe for comments on the manuscript. This work was supported by grants from the PRESTO program of the Japan Science and Technology Agency (JST) (to T.I.), the CREST program of JST (to M.S.), the Mitsubishi Foundation (to T.I.), the Strategic Programs for R&D (President's Discretionary Fund) of RIKEN (to T.I.), the JSPS KAKENHI (grant numbers 23680038 and 15K14336 to T.I., 25111707 and 24300120 to M.S., and 26650072 to T.S.K), and RIKEN CDB intramural grant (to T.I. and T.S.K.). M.-T.K. was supported by RIKEN Foreign Postdoctoral Researcher program. The imaging experiments were supported by the RIKEN Kobe Light Microscopy Facility. Animal experiments were supported by LARGE. We are grateful to Olympus, Carl Zeiss Microscopy, and Leica Microsystems for generously providing chances to use their commercialized super-resolution microscopes. M.-T.K. and T.I. have filed a patent application on SeeDB2, assigned to RIKEN.

Received: July 15, 2015
Revised: January 11, 2016
Accepted: February 9, 2016
Published: March 10, 2016

REFERENCES

Abe, T., Kiyonari, H., Shioi, G., Inoue, K., Nakao, K., Aizawa, S., and Fujimori, T. (2011). Establishment of conditional reporter mouse lines at ROSA26 locus for live cell imaging. Genesis *49*, 579–590.

Baho, E., and Di Cristo, G. (2012). Neural activity and neurotransmission regulate the maturation of the innervation field of cortical GABAergic interneurons in an age-dependent manner. J. Neurosci. *32*, 911–918.

(C) Super-resolution (Airyscan) images of the medulla of the *bsh-Gal4 UAS-CD8GFP* flies, mounted in VECTASHIELD or SeeDB2S and imaged with an oil-immersion lens. Note that bouton-like structures of Mi1 neurons are clearly visualized in SeeDB2S. Both images were taken at 100–120 μm depth.
(D) A super-resolution image of a single Mi1 neuron (*R95A09-Gal4 UAS-myrGFP*). Dendritic processes at M1 and M5 and axon branches at M9–10 layers are visualized.
(E) Super-resolution images of Mi1 axons revealed tripartite structures (*R48E09-Gal4 UAS-myrGFP*). The number of branches ranged from two to four (n = 51 neurons). Axon shafts and axonal branches are indicated by yellow and red arrows, respectively.
(F) Angular orientations of Mi1 axonal boutons are color coded in the reconstruction images (*R48E09-Gal4 UAS-myrGFP*). Angles were not determined for gray neurons.
(G) Angular orientations of M1 dendrite (n = 46), M5 dendrite (n = 46), and M9–10 axonal branches (n = 65) relative to the axonal shaft. Orientations of the center of mass (blue dots) relative to the axon shafts (red) were determined at each layer.
(H) Schematic representation of the fly motion detection circuit. Each of the four types of T4 neurons are tuned to one of the four distinct directions of motion. These four types of T4 neurons are known to show distinct dendritic orientations in M10 layer. Thus, various axonal bouton orientations found in Mi1 neurons may be related to the directional tuning of post-synaptic T4 neurons.
See also Movie S7. A, anterior; P, posterior. Scale bars represent 50 μm in (A) and (B) and 5 μm in (C)–(G). ***$p < 0.001$ (Mardia-Watson-Wheeler test).

Borst, A., and Helmstaedter, M. (2015). Common circuit design in fly and mammalian motion vision. Nat. Neurosci. *18*, 1067–1076.

Chen, J.L., Villa, K.L., Cha, J.W., So, P.T.C., Kubota, Y., and Nedivi, E. (2012). Clustered dynamics of inhibitory synapses and dendritic spines in the adult neocortex. Neuron *74*, 361–373.

Chen, B.C., Legant, W.R., Wang, K., Shao, L., Milkie, D.E., Davidson, M.W., Janetopoulos, C., Wu, X.S., Hammer, J.A., 3rd, Liu, Z., et al. (2014). Lattice light-sheet microscopy: imaging molecules to embryos at high spatiotemporal resolution. Science *346*, 1257998.

Chen, F., Tillberg, P.W., and Boyden, E.S. (2015). Optical imaging. Expansion microscopy. Science *347*, 543–548.

Chung, K., Wallace, J., Kim, S.Y., Kalyanasundaram, S., Andalman, A.S., Davidson, T.J., Mirzabekov, J.J., Zalocusky, K.A., Mattis, J., Denisin, A.K., et al. (2013). Structural and molecular interrogation of intact biological systems. Nature *497*, 332–337.

Ding, J.B., Takasaki, K.T., and Sabatini, B.L. (2009). Supraresolution imaging in brain slices using stimulated-emission depletion two-photon laser scanning microscopy. Neuron *63*, 429–437.

Feng, G., Mellor, R.H., Bernstein, M., Keller-Peck, C., Nguyen, Q.T., Wallace, M., Nerbonne, J.M., Lichtman, J.W., and Sanes, J.R. (2000). Imaging neuronal subsets in transgenic mice expressing multiple spectral variants of GFP. Neuron *28*, 41–51.

Hama, H., Kurokawa, H., Kawano, H., Ando, R., Shimogori, T., Noda, H., Fukami, K., Sakaue-Sawano, A., and Miyawaki, A. (2011). Scale: a chemical approach for fluorescence imaging and reconstruction of transparent mouse brain. Nat. Neurosci. *14*, 1481–1488.

Hama, H., Hioki, H., Namiki, K., Hoshida, T., Kurokawa, H., Ishidate, F., Kaneko, T., Akagi, T., Saito, T., Saido, T., and Miyawaki, A. (2015). ScaleS: an optical clearing palette for biological imaging. Nat. Neurosci. *18*, 1518–1529.

Hasegawa, E., Kitada, Y., Kaido, M., Takayama, R., Awasaki, T., Tabata, T., and Sato, M. (2011). Concentric zones, cell migration and neuronal circuits in the Drosophila visual center. Development *138*, 983–993.

Hayashi, S., and Okada, Y. (2015). Ultrafast superresolution fluorescence imaging with spinning disk confocal microscope optics. Mol. Biol. Cell *26*, 1743–1751.

Hell, S., Reiner, G., Cremer, C., and Stelzer, E.H.K. (1993). Aberrations in confocal fluorescence microscopy induced by mismatches in refractive index. J. Microsc. *169*, 391–405.

Huff, J. (2015). The Airyscan detector from ZEISS: confocal imaging with improved signal-to-noise ratio and super-resolution. Nat. Methods *12*, i–ii.

Kasthuri, N., Hayworth, K.J., Berger, D.R., Schalek, R.L., Conchello, J.A., Knowles-Barley, S., Lee, D., Vázquez-Reina, A., Kaynig, V., Jones, T.R., et al. (2015). Saturated reconstruction of a volume of neocortex. Cell *162*, 648–661.

Ke, M.-T., and Imai, T. (2014). Optical clearing of fixed brain samples using SeeDB. Curr. Protoc. Neurosci. *66*, 2.22.1–2.22.19.

Ke, M.T., Fujimoto, S., and Imai, T. (2013). SeeDB: a simple and morphology-preserving optical clearing agent for neuronal circuit reconstruction. Nat. Neurosci. *16*, 1154–1161.

Kitajima, T.S., Ohsugi, M., and Ellenberg, J. (2011). Complete kinetochore tracking reveals error-prone homologous chromosome biorientation in mammalian oocytes. Cell *146*, 568–581.

Kleinfeld, D., Bharioke, A., Blinder, P., Bock, D.D., Briggman, K.L., Chklovskii, D.B., Denk, W., Helmstaedter, M., Kaufhold, J.P., Lee, W.C.A., et al. (2011). Large-scale automated histology in the pursuit of connectomes. J. Neurosci. *31*, 16125–16138.

Lichtman, J.W., and Denk, W. (2011). The big and the small: challenges of imaging the brain's circuits. Science *334*, 618–623.

Livet, J., Weissman, T.A., Kang, H., Draft, R.W., Lu, J., Bennis, R.A., Sanes, J.R., and Lichtman, J.W. (2007). Transgenic strategies for combinatorial expression of fluorescent proteins in the nervous system. Nature *450*, 56–62.

Maisak, M.S., Haag, J., Ammer, G., Serbe, E., Meier, M., Leonhardt, A., Schilling, T., Bahl, A., Rubin, G.M., Nern, A., et al. (2013). A directional tuning map of Drosophila elementary motion detectors. Nature *500*, 212–216.

Maurice, D.M. (1987). Clearing media for the eye. Br. J. Ophthalmol. *71*, 470–472.

Micheva, K.D., and Smith, S.J. (2007). Array tomography: a new tool for imaging the molecular architecture and ultrastructure of neural circuits. Neuron *55*, 25–36.

Moneron, G., and Hell, S.W. (2009). Two-photon excitation STED microscopy. Opt. Express *17*, 14567–14573.

Peng, H., Hawrylycz, M., Roskams, J., Hill, S., Spruston, N., Meijering, E., and Ascoli, G.A. (2015). BigNeuron: large-scale 3D neuron reconstruction from optical microscopy images. Neuron *87*, 252–256.

Richardson, D.S., and Lichtman, J.W. (2015). Clarifying tissue clearing. Cell *162*, 246–257.

Schermelleh, L., Heintzmann, R., and Leonhardt, H. (2010). A guide to super-resolution fluorescence microscopy. J. Cell Biol. *190*, 165–175.

Shinomiya, K., Karuppudurai, T., Lin, T.Y., Lu, Z., Lee, C.H., and Meinertzhagen, I.A. (2014). Candidate neural substrates for off-edge motion detection in Drosophila. Curr. Biol. *24*, 1062–1070.

Sigal, Y.M., Speer, C.M., Babcock, H.P., and Zhuang, X. (2015). Mapping synaptic input fields of neurons with super-resolution imaging. Cell *163*, 493–505.

Sigrist, S.J., and Sabatini, B.L. (2012). Optical super-resolution microscopy in neurobiology. Curr. Opin. Neurobiol. *22*, 86–93.

Staudt, T., Lang, M.C., Medda, R., Engelhardt, J., and Hell, S.W. (2007). 2,2′-thiodiethanol: a new water soluble mounting medium for high resolution optical microscopy. Microsc. Res. Tech. *70*, 1–9.

Susaki, E.A., Tainaka, K., Perrin, D., Kishino, F., Tawara, T., Watanabe, T.M., Yokoyama, C., Onoe, H., Eguchi, M., Yamaguchi, S., et al. (2014). Whole-brain imaging with single-cell resolution using chemical cocktails and computational analysis. Cell *157*, 726–739.

Takemura, S.Y., Bharioke, A., Lu, Z., Nern, A., Vitaladevuni, S., Rivlin, P.K., Katz, W.T., Olbris, D.J., Plaza, S.M., Winston, P., et al. (2013). A visual motion detection circuit suggested by Drosophila connectomics. Nature *500*, 175–181.

Tomer, R., Ye, L., Hsueh, B., and Deisseroth, K. (2014). Advanced CLARITY for rapid and high-resolution imaging of intact tissues. Nat. Protoc. *9*, 1682–1697.

Tønnesen, J., and Nägerl, U.V. (2013). Superresolution imaging for neuroscience. Exp. Neurol. *242*, 33–40.

Tønnesen, J., Katona, G., Rózsa, B., and Nägerl, U.V. (2014). Spine neck plasticity regulates compartmentalization of synapses. Nat. Neurosci. *17*, 678–685.

Tsien, J.Z., Chen, D.F., Gerber, D., Tom, C., Mercer, E.H., Anderson, D.J., Mayford, M., Kandel, E.R., and Tonegawa, S. (1996). Subregion- and cell type-restricted gene knockout in mouse brain. Cell *87*, 1317–1326.

Ultanir, S.K., Kim, J.E., Hall, B.J., Deerinck, T., Ellisman, M., and Ghosh, A. (2007). Regulation of spine morphology and spine density by NMDA receptor signaling in vivo. Proc. Natl. Acad. Sci. USA *104*, 19553–19558.

Urban, N.T., Willig, K.I., Hell, S.W., and Nägerl, U.V. (2011). STED nanoscopy of actin dynamics in synapses deep inside living brain slices. Biophys. J. *101*, 1277–1284.

Yang, B., Treweek, J.B., Kulkarni, R.P., Deverman, B.E., Chen, C.K., Lubeck, E., Shah, S., Cai, L., and Gradinaru, V. (2014). Single-cell phenotyping within transparent intact tissue through whole-body clearing. Cell *158*, 945–958.